Discontinuous Transition in Electrolyte Flow through Charge-Patterned Nanochannels

Tine Curk [1,*], Sergi G. Leyva [2,3] and Ignacio Pagonabarraga [2,3]

[1]*Department of Materials Science and Engineering, Johns Hopkins University, Baltimore, Maryland 21218, USA*
[2]*Departament de Física de la Matèria Condensada, Universitat de Barcelona, 08028 Barcelona, Spain*
[3]*Universitat de Barcelona Institute of Complex Systems (UBICS), Universitat de Barcelona, 08028 Barcelona, Spain*

We investigate the flow of an electrolyte through a rigid nanochannel decorated with a surface charge pattern. Employing lattice Boltzmann and dissipative particle dynamics methods, as well as analytical theory, we show that the electrohydrodynamic coupling leads to two distinct flow regimes. The accompanying discontinuous transition between slow, ionic, and fast, Poiseuille flows is observed at intermediate ion concentrations, channel widths, and electrostatic coupling strengths. These findings indicate routes to design nanochannels containing a typical aqueous electrolyte that exhibit a digital on-off flux response, which could be useful for nanofluidics and ionotronic applications.

Ion transport through nanochannels often exhibits nonlinear effects such as gating and pressure sensing [1–3]. These mechanisms are generically present in biological nanochannels. For example, channels can adapt their shape in response to mechanical stresses and act as emergency safety valves to avoid cellular damage [4], or change the fluid flows to trigger electrochemical signals [5]. Much effort has been made to mimic the capabilities of such biological mechanisms. For example, conical nanopores with constant surface charge exhibit gating as a function of the exerted pressure, and have been extensively characterized, both experimentally and theoretically [6–12]. Such geometrical asymmetries can result in rectification [6,7] and particle separation due to entropic transport [13]. Both molecular sized pores and nanochannels can give rise to gating and rectification, but the precise response and the physical mechanisms at play may change drastically [8–11,14–16].

An alternative avenue to obtain nonlinear response is by introducing charge heterogeneities. Theoretical investigations indicate that a discontinuity in the surface charge causes a disturbance in the flow profile that can extend a distance from the surface an order of magnitude larger than the Debye screening length λ_D [17]. Indeed, surface charge patterns in micron-sized channels can result in intricate electro-osmotic flows [18] and complex flow patterns such as vortex formation that enhance fluid mixing [19–21]. Hence, surface charge patterns can qualitatively alter electrokinetic flows, opening up the possibility to exploit this feature to control ionic transport in nanochannels.

Here we investigate the flow of an electrolyte through a nanochannel slit of width w at low Reynolds numbers (Re $\ll$ 1). In the absence of charge, pressure-driven flow through a channel with slip length ℓ_s attains the parabolic, Poiseuille velocity profile,

$$v_x^P(y) = \frac{G_x}{2\eta}(w^2/4 - y^2 + w\ell_s), \qquad (1)$$

where G_x is the pressure gradient in the x coordinate, η the dynamic viscosity, and the channel walls are positioned at $y = \pm w/2$. Charging the surface modifies this flow profile due to electrokinetic coupling between the hydrodynamic flow and electrostatic interactions. The electrostatic interaction strength is controlled by the Bjerrum length $l_B = e_0^2/(4\pi\varepsilon_0\varepsilon_r k_B T)$, with e_0 the elementary charge, ε_0 and ε_r the vacuum and relative permittivity, respectively, k_B the Boltzmann constant, and T the absolute temperature, which yields a typical length $l_B = 0.71$ nm for an aqueous solution at room temperature. We employ the simplest charge pattern that preserves charge neutrality: an alternating pattern of positive and negative charged sections with pattern size l and fraction of the surface f with symmetric surface charge density, $\sigma^+ = -\sigma^- = \sigma$ (Fig. 1). The channel contains a symmetric monovalent electrolyte solution at density ρ and ion concentration $c_{ion} = c_{cation} = c_{anion}$. To investigate how the surface charge affects the flow we employ two independent computational methods that combine hydrodynamics with electrostatics, lattice Boltzmann (LB) with electrokinetics [22] and dissipative-particle dynamics (DPD) [23] with explicit ions [24]. The analysis is further supported by analytical mean-field theory.

We initially focus on the parameters corresponding to a channel width $w = 5.16$ nm, containing an aqueous salt solution ($\rho = 10^3$ kg/m³, $\eta = 10^{-3}$ Pa s, $T = 293$ K) and consider a typical slip length ℓ_s for electrolytes on surfaces with different degree of polarity, which is generally small,
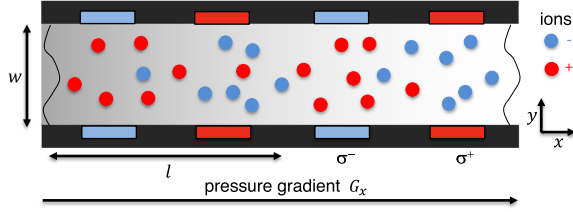
*tcurk@jhu.edu

FIG. 1. Schematic of an electrolyte flow through a charge-patterned nanochannel under a pressure gradient G_x. Channel width w with a charge pattern of size l of alternating positive σ^+ and negative σ^- charge density.

$\ell_s \approx 20$ nm [25,26]. The surface charge pattern length is $l = 5w$ with $f = 0.5$, which makes the width of each charged strip comparable to the width of the channel (Fig. 1). The pattern charge density is $\sigma = 0.05e_0/(\Delta x)^2 \approx \pm 0.5e_0/\text{nm}^2$, which is typical of, e.g., silica or iron oxide surfaces [27].

The LB method combined with a convection-diffusion solver for ions [22] allows us to analyze the steady-state flow of an electrolyte as a function of pressure gradient G_x and ion concentration c_{ion} (Fig. 2). To model small ion diffusion with typical diffusion constant $D \approx 10^{-9}$ m^2/s, we set $D = 10^{-3}\nu$, with the kinematic viscosity $\nu = \eta/\rho$. The slip length is introduced using a fractional bounceback boundary condition at the walls [28]. The lattice size is set to $\Delta x = w/16$, which is sufficiently small to avoid finite size effects [see Supplemental Material (SM) [29]], and the reduced viscosity is set to $\eta^* = 0.2$, which determines the LB time unit $\Delta t = \Delta x^2 \eta^*/\nu$.

Surprisingly, we find that at a threshold pressure gradient G_t, the flow velocity exhibits a discontinuous transition characterized by nearly an order of magnitude change in the average flow velocity [Fig. 2(a)]. This transition is associated with a discontinuous change in the ion distribution measured by the net charge density ρ_q in the channel. The slow flow regime shows localized counterion clouds that reflect the surface charge pattern [Fig. 2(b)], whereas the charge density is largely uniform in the fast flow regime with only a scant signature of the counterion layer [Fig. 2(c)]. This suggest that at $G_x < G_t$ the counterions are localized in a pattern reflecting the surface charge, which results in a high drag on the fluid and thus a distinct slow flow regime. Conversely, at $G_x > G_t$, the drag becomes sufficiently large to pull the counterions away from the patterned surface charge, leading to ion mixing and associated reduction in local net charge density, which in turn substantially reduces the ion drag and results in a discontinuous transition. For $G \gg G_t$, electrokinetic effects become negligible and the average flow velocity is determined by the Poiseuille flow:

$$v_P = \langle v_x^P(y) \rangle = \frac{G_x w^2}{12\eta}\left(1 + \frac{6\ell_s}{w}\right). \qquad (2)$$

The discontinuous transition is observed only at intermediate ion concentrations, whereas both higher and lower
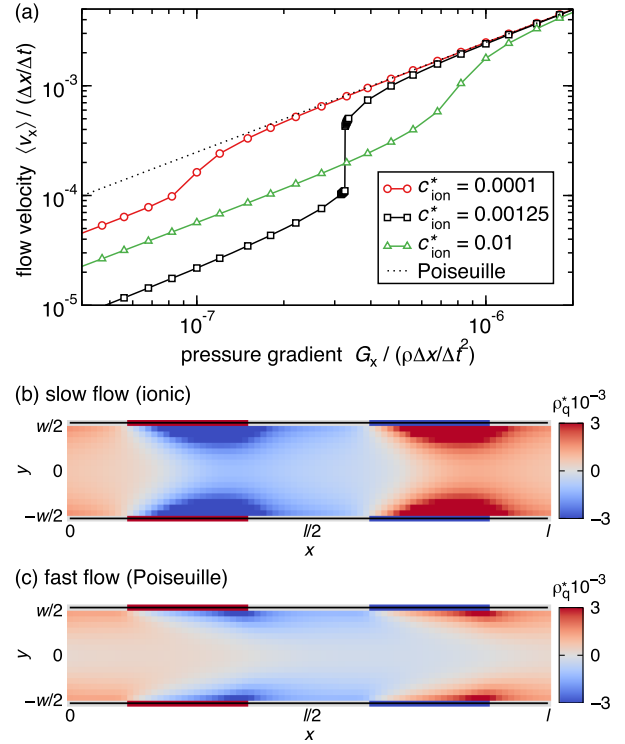

FIG. 2. Steady-state flow velocity obtained from LB simulations. (a) Average velocity at different ion concentrations, $c_{\text{ion}}^* = c_{\text{ion}}\Delta x^3 = [0.0001, 0.001\,25, 0.01]$, corresponding to the Debye length relative to channel width, $\lambda_D/w = [0.83, 0.24, 0.08]$. The dashed line corresponds to ideal Poiseuille flow [Eq. (2)]. (b),(c) Net charge density, $\rho_q^* = \rho_q \Delta x^3/e_0$, at coexistence conditions for the (b) slow and (c) fast flow profiles at $G_x = 3.25 \times 10^{-7}\rho\Delta x/\Delta t^2$ and $G_x = 3.26 \times 10^{-7}\rho\Delta x/\Delta t^2$, respectively. $c_{\text{ion}}^* = 0.00125$, $\sigma = 0.05e_0/(\Delta x)^2$.

salt concentrations result in a nonlinear, but continuous, flow dependence on G_x. This peculiar behavior is a consequence of many-body electrokinetic effects. At low ion concentrations, $c_{\text{ion}} \to 0$, electrostatic interactions become irrelevant and the flow attains the Poiseuille profile. In the opposite limit the electrostatic effects become confined to a narrow boundary layer since $\lambda_D = (8\pi l_B c_{\text{ion}})^{-1/2}$. Conversely, at intermediate ion concentrations the counterion clouds from the opposite walls partially overlap and electrokinetic effects lead to a discontinuous transition that separates the fast and slow flow regimes. The same argument implies the transition occurs only at intermediate Bjerrum lengths. Moreover, to observe the transition, we expect the charge pattern length l should be larger than the Debye length, $l > \lambda_D$, otherwise, neighboring counterion clouds overlap and are neutralized.

Although the LB calculations clearly point to a discontinuous transition in the flow, the method does not include thermal fluctuations and assumes a continuous charge distribution. To establish whether the observed transition is affected by thermal fluctuations or unit charge

discretization, we turn to DPD, which is an off-lattice method that models the solvent as a fluid of soft particles and allows the introduction of explicit ions.

We use standard DPD parameters corresponding to an aqueous solution [23,30] with DPD particle density $\rho_s = 3/\lambda^3$, at $\lambda = 0.645$ nm, and hydrodynamic coupling $\gamma = 4.5 k_B T \tau / \lambda^2$. We introduce electrolyte ions as charged spheres with diameter $\lambda_{ion} = \lambda$ [Fig. 3(a)]. The short-range ion-ion and ion-wall repulsion is modeled using the standard Weeks-Chandler-Andersen potential with strength $\varepsilon = k_B T$. The same Weeks-Chandler-Andersen form is used to describe the smooth channel wall interaction with DPD particles and ions. To separate thermodynamic and hydrodynamic parameters, ions and DPD particles have no conservative pair interaction and interact only through the DPD thermostat [24]. The ion-DPD hydrodynamic coupling is set to $\gamma_{ion} = 5\gamma$, which yields the desired diffusion constant of ions, $D \approx 1$ nm^2/ns, where the time unit, $\tau = 0.077$ ns, is determined from reduced viscosity $\eta^*_{DPD} = 0.85$ [30] via $\eta = \eta^*_{DPD} k_B T \tau \lambda^{-3}$. The pressure gradient G_x is introduced as an external body force on the solvent DPD particles. The system size is $L_x = l = 40\lambda$, $L_y = L_z = w = 8\lambda$, with periodic boundary conditions in x and z coordinates. The partial-slip boundary condition at the walls is implemented by introducing immobilized particles at the wall with surface density $\rho_w = \rho_s \lambda$ that interact with DPD particles only via the thermostat with coupling γ_w, which is determined by the desired slip length ℓ_s. Electrostatic interaction are calculated using particle-particle particle-mesh Ewald summation.

Using this DPD model we find that the steady-state flow in a charge-patterned nanochannel exhibits a doubly peaked velocity distribution [Fig. 3(b)] which implies a discontinuous transition between slow and fast flow regimes. Moreover, the transition becomes sharper at higher surface charge densities, in quantitative agreement with LB (Fig. 4). The agreement is remarkable given that LB does not account for either thermal fluctuations or discrete charges. This indicates that the existence and the location of the discontinuous transition is robust and is not sensitive to the details of the model.

Based on the simulation results, we propose a mean-field theory that captures the essential features of the electrohydrodynamic coupling. The flow velocity is determined by both the drag of ions localized in the channel and the viscous drag of the walls. Specifically, the viscous drag force density of the two confining walls F_w is determined by the shear rate at the walls:

$$F_w = 2\eta \left(\frac{\partial v_x}{\partial y} \right)_{y=-w/2}. \qquad (3)$$

The Stokes drag per ion is $F_d = -(k_B T / D) v_{ion}$, where v_{ion} is the velocity of the ion relative to the surrounding fluid. At small pressure gradients ions are confined to the
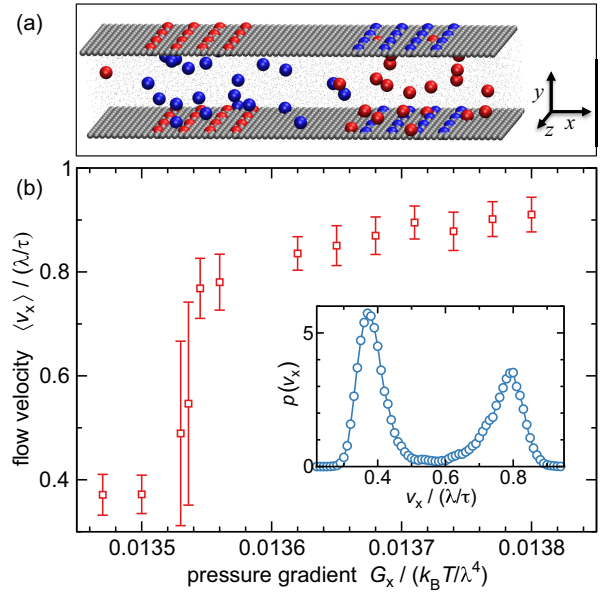

FIG. 3. Steady-state flow from DPD simulations. (a) Nanochannel configuration where cations and anions are shown as red and blue spheres, respectively, while channel walls are shown in gray with embedded surface charges (at $G_x = 0.003 k_B T / \lambda^4$). DPD particles are represented as small black dots. (b) Average velocity; error bars mark the standard deviation of the velocity distribution. Inset shows the velocity distribution at coexistence ($G_x = 0.013\,536 k_B T / \lambda^4$). $c_{ion} = 0.01\lambda^{-3}$ at which $\lambda_D / w = 0.24$.

charged regions [Fig. 3(a)], the relative velocity is thus $v_{ion} = -v_x(y)$. The total ion drag F_i on the fluid is obtained by integrating over all counterions in the charged channel section. Approximating that the counterion charge density ρ_q does not vary with x within each charged section,

$$F_i = \frac{k_B T f}{D} \int_{-w/2}^{w/2} v_x(y) \frac{\rho_q(y)}{e_0} dy, \qquad (4)$$

where $\rho_q(y)/e_0$ is the counterion concentration profile.

We can now analytically estimate the ratio of drag forces due to bound counterions and the channel walls. Assuming the flow profile remains parabolic and the counterion density follows the exponential Debye-Hückel screening profile, we find that for overlapping counterion layers, $\lambda_D > w/3$, and small pressure gradient limit,

$$R' = \frac{F_i}{F_w} = 3\pi \lambda_h \min[\sigma f / e_0, w c_{ion}] \left(\ell_s + \frac{w}{6} \right). \qquad (5)$$

which takes into account that the counterion charge density is limited by the surface charge density or the electrolyte concentration, and the hydrodynamic diameter of ions $\lambda_h = k_B T / (3\pi D \eta)$; see SM for detailed derivation [29]. In the opposite, wide-channel limit we find
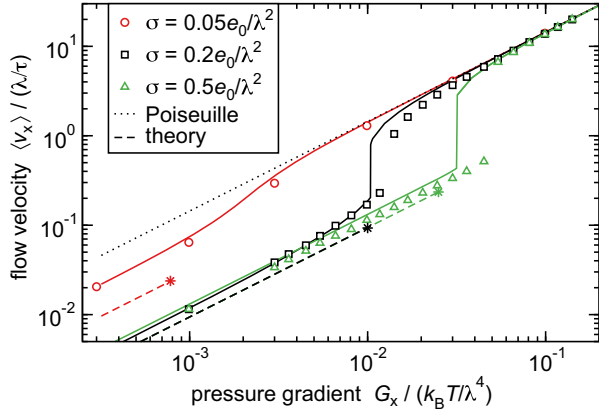
FIG. 4. Steady-state flow at different surface charge densities σ. Comparison between DPD (symbols), LB (solid lines), and analytical prediction for the Poiseuille regime [dotted line, Eq. (2)] and ionic regime [dashed line, Eq. (7)], which terminates at the transition [star symbol, Eq. (8)]. Parameters are $c_{ion} = 0.01\lambda^{-3}$, $\lambda = 2\Delta x$, $\lambda_D/w = 0.24$.

$$R'(\lambda_D < w/3) = 3\pi\lambda_h \min[\sigma f/e_0, wc_{ion}]\left(\ell_s + \frac{\lambda_D}{2}\right). \quad (6)$$

The average flow velocity in the channel $\langle v_x \rangle \propto G_x/(F_w + F_i)$ can be written as

$$\langle v_x \rangle = \frac{v_P}{1 + R}, \quad (7)$$

where $R = R'$ for $G_x < G_t$, and $R = 0$ for $G_x > G_t$, with the transition at G_t. For $R \ll 1$, the ion contribution is negligible and the flow attains the Poiseuile profile [Eqs. (1) and (2)], whereas for $R > 1$, the ion drag dominates and we call this regime "ionic."

The transition between the two flow profiles occurs when the hydrodynamic force is sufficiently large to pull the ions away from the charge pattern. This can be calculated analytically by approximating each surface patch by a line charge and each counterion cloud by another line charge located in the center of the channel (see SM [29]). The transition occurs at a pressure gradient G_t that can overcome the electrostatic restoring force:

$$G_t = \frac{2\sigma f l c_{ion} k_B T l_B}{e_0 w} \min[1, \sigma f/(c_{ion} w e_0)]. \quad (8)$$

This theory is able to semiquantiatively predict both the flow velocity $\langle v_x \rangle$ and the location of the transition G_t (Fig. 4). Moreover, the theory predicts general regions of parameter space where different flow regimes are expected to be observed [Figs. 5(a) and 5(b)], supported by LB simulations data [Figs. 5(c) and 5(d)]. The ionic regime is found at sufficiently large c_{ion} and w, while the discontinuous transition is found only in a limited range of c_{ion} and w at which both ion drag and screening length relative
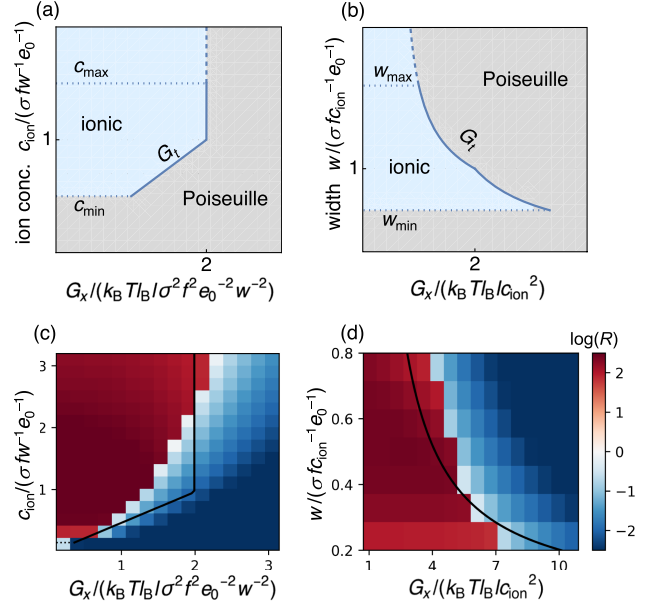

FIG. 5. Diagrams delineating the Poiseuille and ionic flow regimes: (a) constant c_{ion}, (b) constant w. The lower bounds c_{min} and w_{min} (dotted lines) are determined by $R' = 1$ [Eqs. (5) and (6)]. The transition occurs at G_t [Eq. (8)] and is discontinuous (solid line) below c_{max} and w_{max} (determined by $w \approx 10\lambda_D$), and gradual (dashed line) above these bounds. (c),(d) Comparison to LB simulation data showing a heat map of $\log R$, with R computed according to Eq. (7). Parameters are $\sigma = 0.1e_0/(\Delta x)^2$, $f = 0.5$, in (c) $w = 16\Delta x$, while in (d) $c_{ion} = 0.00125/\Delta x^3$.

to channel size are appreciable. The larger the slip length, the larger the relative drag of ions [Eq. (5)] and thus the larger the jump at the transition [Eq. (7)].

For non-neutral charge patterns the fluid attains a net charge and the electro-osmotic flow can be induced by an external electric field E_x instead of a pressure gradient. For a pattern consisting of only one polarity we again observe a discontinuous transition (Fig. 6). The only notable difference is a lower limit for the counterion concentration $\langle \rho_q \rangle = 2f\sigma/w$, at which the transition remains discontinuous even in the absence of extra salt density $c_{ion,ex}$. The net body force, $G_x = E_x \langle \rho_q \rangle$, is determined by the net charge density $\langle \rho_q \rangle$. The location of the transition E_t is well predicted by the theory, $E_t = G_t^s/\langle \rho_q \rangle = 1.4 \times 10^{-4}[\rho(\Delta x)^4/(\Delta t)^2 e_0]$ [for a single polarity charge the transition $G_t^s = G_t/2$ and $\sigma f/(c_{ion} w e_0) \leq 1$; see SM [29]]. Thus, we expect the flow-regime diagrams (Fig. 5) are qualitatively applicable to flows driven by electric fields.

The observed flow transition occurs at pressure gradient $G_t \approx 10^{-2} k_B T/\lambda^4 \approx 2$ bar/nm in Figs. 2–4, and electric field $E_t \approx 10^{-4}\rho(\Delta x)^4/[e_0(\Delta t^2)] \approx 20$ mV/nm (Fig. 6), both of which are very large. These values can be substantially reduced by increasing the slip length ℓ_s [see Eqs. (5) and (8) and Fig. 5]. For example, at constant
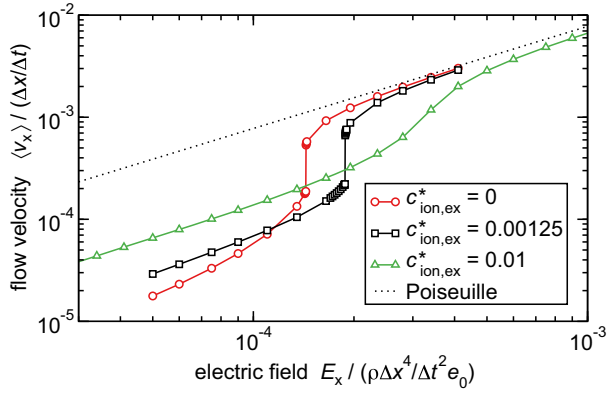
FIG. 6. Steady-state flow velocity for electric field driven flow at $\sigma = 0.1 e_0/\Delta x^2$. The channel configuration is the same as shown in Fig. 2, but without the negative surface charge. The dashed line corresponds to ideal Poiseuille flow [Eq. (2)] at force density $G_x = E_x \langle \rho_q \rangle$.

c_{ion} the minimum $G_t \propto \ell_s^{-2}$. For a superhydrophobic surface ($\ell_s = 10$ μm) [26,31], we predict a minimum $G_t \approx 0.01$ bar/μm and $E_t \approx 40$ mV/μm. Conversely, the distinct flow regimes are observed even if the slip length is smaller than channel width, $\ell_s < w$, although in this case the transition is not discontinuous (see SM [29]).

In summary, we have investigated the flow of an electrolyte solution through a rigid nanochannel decorated with a surface charge pattern and demonstrated the capability of effective gating for overall electroneutral channels. Simulation results and analytical theory predict two distinct flow regimes, a slow ion-drag dominated flow, and a faster Poiseuille flow, separated by a discontinuous transition. This discontinuous transition occurs only at intermediate ion concentrations, channel widths, and electrostatic coupling strengths and appears to be qualitatively different from both the Coulomb blockade effect [32] in nanochannels and the continuous laminar-turbulent transition in pipe flow [33].

While mechanosensitive nanochannels are common in biology, their nonlinear response is typically coupled to structural changes in the channel such as protein conformational changes [34]. Our findings imply that such structural changes are not necessary to obtain two distinct (on-off) flow profiles. Moreover, the principles that drive the discontinuous flow transition open venues for the design of nanochannel devices, an alternative to those based on conical pores [9,12] and angstrom-scale slits [35], that could also result in a memristive response. Hence, the possibility to control ionic transport through charge-patterned nanochannels makes them potential components in iontronics and the design of brain-inspired neuronal circuits.

[1] E. Perozo, M. C. Cortes, P. Sompornpisut, A. Kloda, and B. Martinac, Open channel structure of MscL and the gating mechanism of mechanosensitive channels, Nature (London) **418**, 942 (2002).

[2] S. Sukharev and D. Corey, Mechanosensitive channels: Multiplicity of families and gating paradigms, Sci. STKE **219**, 1 (2004).

[3] N. Bavi, M. C. Cortes, C. Cox, P. Rohde, W. Liu, J. Deitmer, O. Bavi, P. Strop, A. Hill, D. Rees, B. Corry, E. Perozo, and B. Martinac, The role of MscL amphipathic N terminus indicates a blueprint for bilayer-mediated gating of mechanosensitive channels, Nat. Commun. **7**, 11984 (2016).

[4] E. Haswell, R. Phillips, and D. Rees, Mechanosensitive channels: What can they do and how do they do it?, Structure **19**, 1356 (2011).

[5] B. Martinac and O. Hamill, Gramicidin a channels switch between stretch activation and stretch inactivation depending on bilayer thickness, Proc. Natl. Acad. Sci. U.S.A. **99**, 4308 (2002).

[6] Z. Siwy, E. Heins, C. Harrell, P. Kohli, and C. Martin, Conical-nanotube ion-current rectifiers: The role of surface charge, J. Am. Chem. Soc. **126**, 10850 (2004).

[7] C. C. Harrell, P. Kohli, Z. Siwy, and C. R. Martin, DNA-nanotube artificial ion channels, J. Am. Chem. Soc. **126**, 15646 (2004).

[8] J. Cervera, B. Schiedt, and P. Ramirez, A Poisson/Nernst-Planck model for ionic transport through synthetic conical nanopores, Europhys. Lett. **71**, 35 (2007).

[9] L. Jubin, A. Poggioli, A. Siria, and L. Bocquet, Dramatic pressure-sensitive ion conduction in conical nanopores, Proc. Natl. Acad. Sci. U.S.A. **115**, 4063 (2018).

[10] T.-W. Lin and J.-P. Hsu, Pressure-driven energy conversion of conical nanochannels: Anomalous dependence of power generated and efficiency on *p*H, J. Colloid Interface Sci. **564**, 491 (2019).

[11] S. Dal Cengio and I. Pagonabarraga, Confinement-controlled rectification in a geometric nanofluidic diode, J. Chem. Phys. **151**, 044707 (2019).

[12] T. M. Kamsma, W. Q. Boon, T. ter Rele, C. Spitoni, and R. van Roij, Iontronic neuromorphic signaling with conical microfluidic memristors, Phys. Rev. Lett. **130**, 268401 (2023).

[13] P. Malgaretti, I. Pagonabarraga, and J. M. Rubi, Entropic electrokinetics: Recirculation, particle separation, and negative mobility, Phys. Rev. Lett. **113**, 128301 (2014).

[14] M. Ghosh, K. F. A. Jorissen, J. A. Wood, and R. G. H. Lammertink, Ion transport through perforated graphene, J. Phys. Chem. Lett. **9**, 6339 (2018).

[15] L. Xie, J. Tang, R. Qin, Q. Zhang, J. Liu, Y. Jin, and H. Wang, Surface charge modification on 2D nanofluidic membrane for regulating ion transport, Adv. Funct. Mater. **33,** 2208959 (2023).

[16] Z. Zhu, D. Wang, Y. Tian, and L. Jiang, Ion/molecule transportation in nanopores and nanochannels: From critical principles to diverse functions, J. Am. Chem. Soc. **141,** 8658 (2019).

[17] A. S. Khair and T. M. Squires, Surprising consequences of ion conservation in electro-osmosis over a surface charge discontinuity, J. Fluid Mech. **615,** 323 (2008).

[18] A. D. Stroock, M. Weck, D. T. Chiu, W. T. S. Huck, P. J. A. Kenis, R. F. Ismagilov, and G. M. Whitesides, Patterning electro-osmotic flow with patterned surface charge, Phys. Rev. Lett. **84,** 3314 (2000).

[19] S. Datta and J. N. Choudhary, Effect of hydrodynamic slippage on electro-osmotic flow in zeta potential patterned nanochannels, Fluid Dyn. Res. **45,** 055502 (2013).

[20] L. M. Lee, W. L. W. Hau, Y.-K. Lee, and Y. Zohar, In-plane vortex flow in microchannels generated by electroosmosis with patterned surface charge, J. Micromech. Microeng. **16,** 17 (2005).

[21] U. Ghosh and S. Chakraborty, Patterned-wettability-induced alteration of electro-osmosis over charge-modulated surfaces in narrow confinements, Phys. Rev. E **85,** 046304 (2012).

[22] F. Capuani, I. Pagonabarraga, and D. Frenkel, Discrete solution of the electrokinetic equations, J. Chem. Phys. **121,** 973 (2004).

[23] R. D. Groot and P. B. Warren, Dissipative particle dynamics: Bridging the gap between atomistic and mesoscopic simulation, J. Chem. Phys. **107,** 4423 (1997).

[24] T. Curk, Dissipative particle dynamics for coarse-grained models, J. Chem. Phys. **160,** 174115 (2024).

[25] P. Joseph and P. Tabeling, Direct measurement of the apparent slip length, Phys. Rev. E **71,** 035303(R) (2005).

[26] L. Bocquet and E. Charlaix, Nanofluidics, from bulk to interfaces, Chem. Soc. Rev. **39,** 1073 (2010).

[27] G. Trefalt, S. H. Behrens, and M. Borkovec, Charge regulation in the electrical double layer: Ion adsorption and surface interactions, Langmuir **32,** 380 (2016).

[28] K. Wolff, D. Marenduzzo, and M. E. Cates, Cytoplasmic streaming in plant cells: The role of wall slip, J. R. Soc. Interface **9,** 1398 (2012).

[29] See Supplemental Material at http://link.aps.org/supplemental/10.1103/PhysRevLett.133.078201 for simulation details, analytical derivations and supporting data.

[30] A. Boromand, S. Jamali, and J. M. Maia, Viscosity measurement techniques in dissipative particle dynamics, Comput. Phys. Commun. **196,** 149 (2015).

[31] C. Ybert, C. Barentin, C. Cottin-Bizonne, P. Joseph, and L. Bocquet, Achieving large slip with superhydrophobic surfaces: Scaling laws for generic geometries, Phys. Fluids **19,** 123601 (2007).

[32] N. Kavokine, S. Marbach, A. Siria, and L. Bocquet, Ionic Coulomb blockade as a fractional Wien effect, Nat. Nanotechnol. **14,** 573 (2019).

[33] M. Sano and K. Tamai, A universal transition to turbulence in channel flow, Nat. Phys. **12,** 249 (2016).

[34] C. D. Cox, N. Bavi, and B. Martinac, Biophysical principles of ion-channel-mediated mechanosensory transduction, Cell Rep. **29,** 1 (2019).

[35] P. Robin, N. Kavokine, and L. Bocquet, Modeling of emergent memory and voltage spiking in ionic transport through angstrom-scale slits, Science **373,** 687 (2021).

[36] http://www.rockfish.jhu.edu